# Model Studies of the Wind-Driven Transient Circulation in the Middle Atlantic Bight. Part 1: Adiabatic Boundary Conditions[1]

ROBERT C. BEARDSLEY AND DALE B. HAIDVOGEL

*Department of Physical Oceanography, Woods Hole Oceanographic Institution, Woods Hole, MA 02543*

(Manuscript received 4 February 1980, in final form 22 December 1980)

ABSTRACT

A numerical model of the wind-driven transient ocean circulation in the Middle Atlantic Bight is described. The model incorporates realistic topography and covers the continental shelf between the coast and the 200 m isobath from Cape Hatteras to the southern tip of Nova Scotia. The traditional shallow-water dynamics are used, i.e., the vertically integrated and linearized equations for the flow of a homogeneous fluid driven by atmospheric pressure and wind stress fluctuations and damped by a quadratic bottom stress. The equations are integrated in time using a simple modification of Platzman's (1972) finite-difference scheme, with a 12.7 km grid spacing. At the coast, normal flow is required to vanish; at non-coastal boundaries, the equivalent surface elevation is held fixed.

Several classes of initial value experiments are used to study the free and forced modes of this model, and the damped flow driven by a spatially uniform and stationary wind stress and by an idealized traveling synoptic-scale wind-stress pattern. The numerical experiments indicate that several time scales are important in the regional adjustment process. These are an inertial time scale dependent on the regional long-wave propagation speed, a local frictional time scale dependent on the strength of the depth-averaged velocity field, and a longer time scale which reflects the adjustment process within the entire model. The transient response within the Middle Atlantic Bight proper from Cape Cod to Cape Hatteras to an alongshore wind stress is clearly dominated by friction and rotation. The effective spinup time scale for a 2 dyn $cm^{-2}$ wind stress is about 10 h at New York. This is sufficiently short in comparison to the 4–10 day time scales characterizing atmospheric transients that the storm-driven currents should be quasi-steady. Within the deeper Gulf of Maine basin, the effective spinup time scale is much longer and the normal modes of the basin excited by the wind forcing are only weakly damped in time.

A comparison of model and observational data on current and sea level variability indicates that the model response is more realistic within the Middle Atlantic Bight section of the model domain. Differences within the Gulf of Maine are due primarily to the specific boundary condition imposed on the upcoast (Scotian shelf) boundary.

## 1. Introduction

Recent direct current measurements made in the Middle Atlantic Bight (MAB) demonstrate that the mean alongshore flow is directed downcoast towards the southwest from Cape Cod to Cape Hatteras. (See Fig. 1 for a map of the MAB.) The mean alongshore currents typically range from 2–8 cm $s^{-1}$ and are presently believed to be driven against an opposing mean wind stress (with a small upcoast component) by an alongshelf pressure gradient imposed at the shelf break by the large-scale cyclonic gyre in the western North Atlantic (see Csanady, 1980; Beardsley and Winant, 1979).

The atmospheric forcing over this shelf region is highly variable, however. Using the NODC collection of ship weather data, Saunders (1977) found that the average standard deviation of wind stress during winter (December–February) varies from about 1.5 dyn $cm^{-2}$ nearshore to 3.0 dyn $cm^{-2}$ offshore near the shelf break. The mean stress during this winter period is directed roughly toward the ESE and varies from 0.75 dyn $cm^{-2}$ nearshore to 1.25 dyn $cm^{-2}$ near the shelf break. Most of the wind-stress variance is caused by a succession of intense low-pressure disturbances or winter cyclones which grow in strength as they move eastward up the coast. Mooers *et al.* (1976) have examined coastal weather data and estimate that the surface wind stress and atmospheric pressure fields are coherent over length scales of 500 and 1500 km, respectively. Direct current measurements obtained with moored instrument arrays show that the alongshore current and transport fluctuations are strongly wind-driven and spatially coherent in the 0.1 to 0.5 cpd band. The magnitudes of these wind-driven alongshore current transients typically vary between 25 and 50 cm $s^{-1}$.

These direct current measurements show that much of the subtidal current variability observed in

[1] Woods Hole Oceanographic Institution Contribution No. 4520.

0022-3670/81/030355-21$09.25

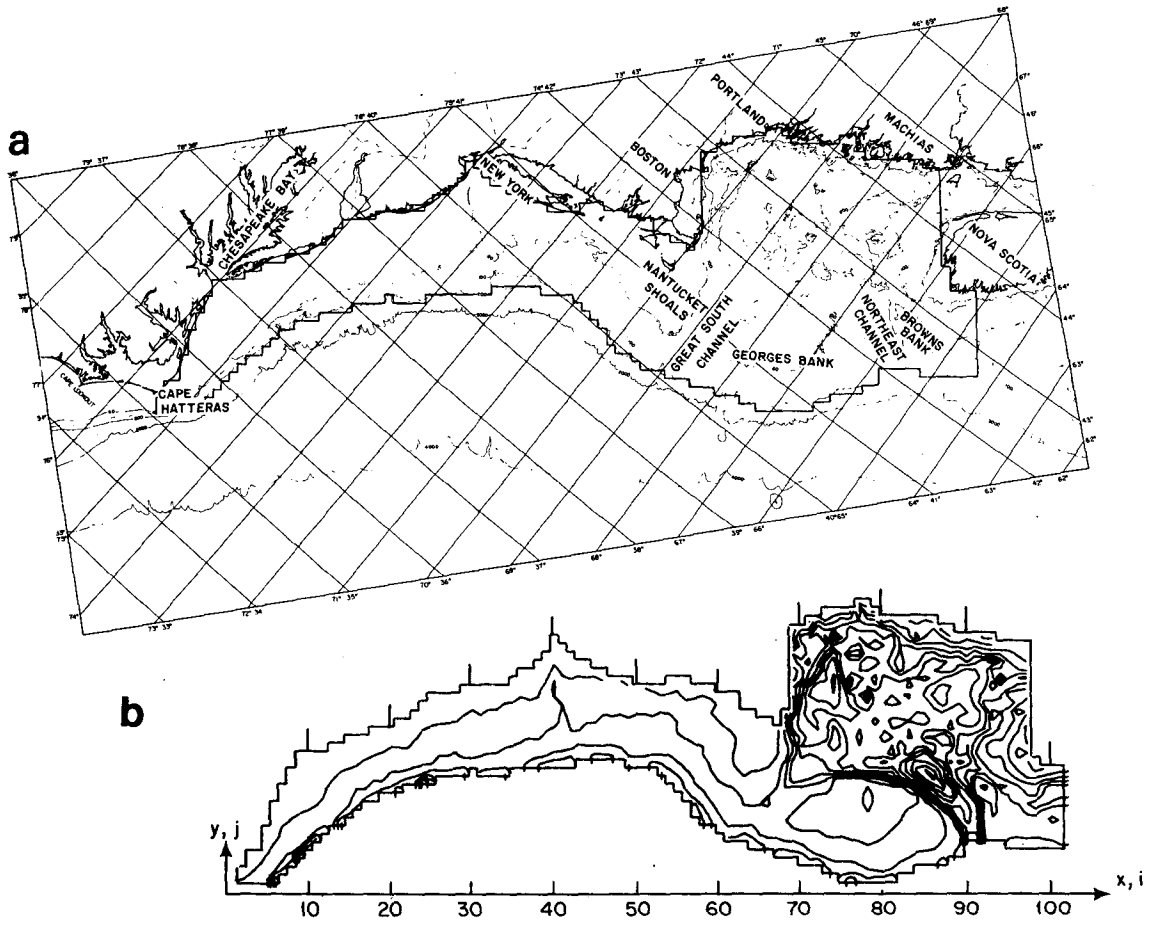


FIG. 1. Topographic map of Middle Atlantic Bight and Gulf of Maine region showing: (a) outline of model domain, and (b) model topography and coordinate system. The contour interval for depth in (b) is 30 m.

the MAB (especially over the shallower sections) is directly wind driven. A simple Ekman model suggested by Beardsley and Butman (1974) correctly describes in a crude qualitative sense the response of this region to strong wind events. A winter storm passing to the south and east of the MAB produces a strong wind stress directed toward the southwest over the shelf, roughly parallel to the coast from Cape Cod to Cape Hatteras. Geostrophic adjustment to the southwest flow causes sea level to rise along the coast. Sea level over the upper slope remains nearly constant on the atmospheric synoptic time scale so that the coastal rise in sea level represents a coastal-trapped onshore pressure gradient in approximate geostrophic balance with the strong alongshore flow. Noble and Butman (1979), Bennett and Magnell (1979) and Wang (1979) have recently examined the response of coastal sea level and nearshore currents in the MAB to winds and suggest that the observed wind-driven transient behavior is more complex than that predicted by a two-dimensional Ekman model. All three investigations indicate that the alongshore setup effects occur in the MAB, especially in the New York Bight where the coastline has a relatively sharp bend near New York City.

To study the cumulative effects of coastline geometry and realistic topography, rotation and bottom friction on the wind-driven transient circulation in the MAB, we have constructed a simple numerical model to solve the traditional shallow-water dynamical equations in a domain covering the continental shelf between the coast and the upper slope from Cape Hatteras to the southern tip of Nova Scotia. The physical and computational details of the model are described in Section 2. Using a particularly simple boundary condition on the noncoastal model boundaries, a sequence of initial value experiments has been conducted to determine: 1) the local and global adjustment time-scales within the MAB; 2) the accompanying spatial structure of surface elevation and horizontal transport fields; and 3) the dynamic (momentum) balances characterizing the transient circulation. The global modes of oscillation of the MAB model are described in Section 3.

The free local response of the MAB to initial non-equilibrium sea level distributions is examined in Section 4. Finally, the character of the wind-driven transient circulation is determined both for steady, spatially uniform winds (Section 5) and idealized moving storms of finite lateral extent (Section 6). The results of these calculations are compared with available field observations in Section 7.

The reliability of these simulations is limited primarily by the uncertainty associated with the specification of an open boundary condition on the cross-shelf and shelf-break boundaries. Preliminary results of a boundary condition sensitivity study indicate that, while the local adjustment time-scales within the MAB may be relatively insensitive to the cross-shelf boundary conditions, adjustment on longer time-scales is strongly constrained by the specific choice of these conditions. Part II of this paper will present a quantitative description of these sensitivity tests.

## 2. The numerical model

We consider the vertically-integrated and linearized momentum and continuity equations for the flow of a homogeneous fluid driven by atmospheric pressure and wind stress, and damped by a quadratic bottom stress:

$$\mathbf{U}_t + f \times \mathbf{U} = -gh\nabla(\zeta + \zeta_a) + (\tau_a - \tau_b), \quad (1)$$

$$\zeta_t + \nabla\cdot\mathbf{U} = 0. \quad (2)$$

Here, $\mathbf{U}$ is the vertically integrated velocity or horizontal transport vector, $f$ the Coriolis parameter, $g$ gravity, $h$ the water depth, $\zeta$ the free surface elevation, $\zeta_a$ the atmospheric pressure divided by $\rho g$, $\tau_a$ the kinematic surface wind stress, and $\tau_b$ the kinematic bottom stress given by $C_D|\mathbf{U}|\mathbf{U}/h^2$ with $C_D = 0.0025$.

For boundary conditions, we require that (i) the normal component of the transport vector vanish at the coast (a solid boundary), and (ii) the adjusted surface elevation $(\zeta + \zeta_a)$ remain constant above the open ocean boundary of the model. This second condition (ii) in effect isolates the shelf domain from open ocean forcing processes which can drive shelf currents through alongshelf pressure gradients (Allen, 1976). Clearly an approximation, this boundary condition is crudely consistent with bottom pressure measurements made in the Sargasso Sea by Brown *et al.* (1975) and on the upper New England slope by Brown (1979, personal communication) which demonstrate that the adjusted surface elevation $(\zeta + \zeta_a)$ is constant over the deep ocean and upper slope to within $\pm 1$ cm in the synoptic frequency band from 0.1 to 0.5 cpd. Since the adjusted surface elevation can vary by $\pm 50$ cm at the coast during a major storm and the few direct pressure measurements available over the shelf in the Mid-Atlantic Bight (see Beardsley *et al.*, 1977) suggest a monotonic offshore decrease in subtidal subsurface pressure variability, the conceptual model having a node in the adjusted elevation field over the slope seems a good first approximation.

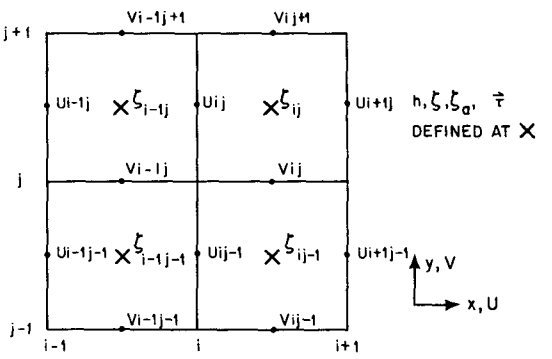


FIG. 2. Location of depth ($h$), atmospheric wind stress ($\tau$), pressure ($\zeta_a$), and dependent variables $U$, $V$, $\zeta$ on a Richardson lattice.

For nearly steady flows in which the local fluid accelerations are not dynamically important, boundary condition (ii) implies that the only transport into the model through the open boundary along the shelf break occurs in the surface Ekman layer driven by the local wind-stress component parallel to the boundary and in the bottom Ekman layer driven by the interior pressure gradient component normal to the boundary. Nearly steady flows parallel to the open boundary can contain both a surface Ekman-layer component and a barotropic geostrophic component associated with the pressure gradient component normal to the boundary.

Condition (ii) is also applied along the cross-shelf boundaries at the northeast and southwest ends of the model. This procedure is intuitively more acceptable at Cape Hatteras where the shelf is relatively narrow. The Scotian Shelf is considerably wider, however, and low-frequency alongshelf flow to the southwest presumably occurs in rough geostrophic balance with a cross-shelf pressure gradient (Smith *et al.*, 1978). We assume as a working hypothesis for this initial model study that inaccuracies attributable to the boundary condition on the Scotian shelf will be spatially limited to the Scotian shelf and Gulf of Maine (abbreviated GOM). Additional numerical experiments using alternate open boundary condition specifications, to be described in Part II of this paper, show this working hypothesis to be only partially justified.

The dependent variables in Eqs. (1) and (2) are defined on a Richardson lattice (also known as the Arakawa C grid; Fig. 2). The transports $U$ and $V$ are defined on the boundary of each grid box while the depth ($h$), wind stress ($\tau$), surface elevation ($\zeta$), and

atmospheric pressure ($\zeta_a$) are defined at the center of each grid box. The grid net has a uniform spacing of $\Delta x = \Delta y = 12.7$ km and grid-point locations $(x_i, y_j) = (i\Delta x, j\Delta y)$, where $i$ and $j$ are the standard grid-point indices. With $U^n$ and $V^n$ defined at $t = n\Delta t$ and the variables $\zeta_T^n = \zeta^n + \zeta_a^n$ and $\tau^n$ defined at $t = (n + 1/2)\Delta t$, a simple modification of Platzman's (1972) integration scheme yields the following finite-difference analogs of Eqs. (1) and (2):

$$U^{n+1} = U^n + f\Delta t\tilde{V}^n - \frac{g\bar{h}^x\Delta t}{\Delta x}\Delta_x\zeta_T^n + \Delta t\overline{\tau_x^n}^x - \frac{\Delta tC_D}{(\bar{h}^x)^2}[(U^n)^2 + (\tilde{V}^n)^2]^{1/2}U^n, \quad (3a)$$

$$V^{n+1} = V^n - f\Delta t\tilde{U}^{n+1} - \frac{g\bar{h}^y\Delta t}{\Delta x}\Delta_y\zeta_T^n + \Delta t\overline{\tau_y^n}^y - \frac{\Delta tC_D}{(\bar{h}^y)^2}[(\tilde{U}^{n+1})^2 + (V^n)^2]^{1/2}v^n, \quad (3b)$$

$$\zeta_{i,j}^{n+1} = \zeta_{ij}^n - \frac{\Delta t}{\Delta x}(\Delta_x U_{i+1,j}^{n+1} + \Delta_y V_{i,j+1}^{n+1}), \quad (4)$$

where the difference and average operators are given by

$$\Delta_x g = g_i - g_{i-1},$$
$$\Delta_y g = g_j - g_{j-1},$$
$$\bar{g}^x = \tfrac{1}{2}(g_i + g_{i-1}),$$
$$\bar{g}^y = \tfrac{1}{2}(g_j + g_{j-1}).$$

Platzman evaluates the Coriolis acceleration term using potential vorticity ($f/h$) as the weights in a spatial averaging procedure. Since we keep $f$ constant in this model, Platzman's procedure reduces to inverse depth averaging so that the Coriolis terms in (3) are defined by

$$\tilde{U}_{ij} = \tfrac{1}{8}\bar{h}_{ij}^y\left[\sum_{m=i}^{i+1}\sum_{n=j-1}^{j}\left(\frac{1}{\bar{h}_{ij}^y} + \frac{1}{\bar{h}_{mn}^x}\right)U_{mn}\right],$$

$$\tilde{V}_{ij} = \tfrac{1}{8}\bar{h}_{ij}^x\left[\sum_{m=i-1}^{i}\sum_{n=j}^{j+1}\left(\frac{1}{\bar{h}_{ij}^x} + \frac{1}{\bar{h}_{mn}^y}\right)V_{mn}\right].$$

This scheme possesses second-order accuracy in both time and space with the exception of the bottom-stress term which is lagged by $\Delta t/2$ in time. The Courant-Friedrichs-Lewy condition for a constant depth basin requires that $\sqrt{gh}\Delta t/\Delta x < 0.70$ for stability or that $\Delta t \leq 150$ s for $h \leq 360$ m. While a maximum depth of 354 m occurs within the model domain in the GOM, the spatial averaging implicit in the finite-difference equations (3.4) reduces the effective depth. All calculations reported in the following sections were integrated using $\Delta t = 150$ s with no apparent computational instabilities. [An experiment conducted with a somewhat larger time step ($\Delta t = 180$ s) did prove, however, to be unstable.]

The model domain (shown enclosed by a heavy boundary in Fig. 1a) is a subsection of a 102 × 36 rectangular grid net which has been superimposed on Uchupi's (1965) topographic map for the eastern continental margin of North America. The origin of the $x$-$y$ coordinate is located at point 0 (34.9°N, 75.1°W) with the $x$-axis oriented toward 51.6°T. The grid net is approximately 1774 km long × 458 km wide.

To simplify the initial coding, we have required the model coastline to be single-valued in the $y$ direction so that features like the Chesapeake and Delaware Bays, Long Island Sound, Massachusetts Bay, and the Bay of Fundy have been excluded. Martha's Vineyard and Nantucket Island have been replaced by the 10 m deep shallows. The open ocean boundary was chosen to follow the 200 m isobath. Grid boxes totally overlying land are arbitrarily assigned a depth of 1 m to avoid division by zero in the expressions for smoothed values of depth. The interior model topography was created by a visual linear interpolation of Uchupi's bathymetry to the model depth grid points. With the exception of islands and regions adjacent to the coastline, no spatial smoothing was done. The 12.7 km grid spacing used was adequate to resolve the relatively smooth topographic variations within the MAB from Cape Cod to Cape Hatteras. The topography within the Gulf of Maine is much more variable and some of the smaller scale features like Cashes Ledge are poorly resolved. The resulting model topography is shown in Fig. 1b.

## 3. Normal mode experiments

Using Platzman's (1972) method, we first determine the lowest inviscid normal modes of the model and of the two main sub-basins (the MAB and GOM). Our motivation here is to clearly identify both the modal shape and period of the lowest normal modes; these modes describe a part of the variability observed in the transient experiments discussed in Section 5.

Garrett (1974) has employed the same numerical technique to examine the lowest normal modes of the GOM separately. His model geometry included the Bay of Fundy and was limited to the northeast and southwest by cross-shelf walls located off Halifax and Nantucket, respectively. Our GOM sub-basin does not include the Bay of Fundy and thus possesses modes which differ from Garrett's results, although our gravest GOM mode is structurally similar to Garrett's second mode (the latter having both a small amplitude response and an amphidromic point located near the Bay of Fundy). Here, we test the implicit assumption that Nantucket Shoals effectively separates the lowest modes in the GOM

TABLE 1. The periods of the lowest GOM and MAB normal modes found in the sub-basins and whole basins.

| Experiment number | Domain $i_{min}$ | Domain $i_{max}$ | Period (h) | Basin |
|---|---|---|---|---|
| NM1 | 65 | 102 | 8.79 | GOM |
| NM2 | 1 | 102 | 10.60 | Full model |
| NM3 | 1 | 65 | 6.70 | MAB |
| NM4 | 1 | 102 | 6.70 | Full model |

from the lowest modes in the MAB by the following sequence of normal mode calculations. A computation is first made to define the lowest mode in each sub-basin. The resulting mode is then used as the initial guess in a search for the lowest modes of the whole model. The results of the four experiments (NM1 to NM4) are shown in Table 1 and Fig. 3.

The lowest normal mode in the GOM sub-basin (without the Bay of Fundy) consists of a counterclockwise movement of the free surface with a period of 8.79 h. This period is significantly increased by 21% to 10.60 h and the modal shape and phase modified in NM2 when the MAB is added. The modal shape and phase of this lowest GOM mode are shown in Fig. 3a. We note, however, that the structure of this gravest GOM mode is *not* sensitive to the placement of the southwestern boundary of the GOM as long as that boundary is positioned more than 100 km west of Nantucket Shoals. When the southwestern boundary coincides with $i = 60$ for instance, the period of the lowest GOM mode has increased to 10.56 h, nearly its "true" value. It remains to be seen if the inclusion of the New England shelf in Garrett's model domain would significantly change the period of his lowest mode, and hence his conclusions about the resonant behavior of the Gulf of Maine to the $M_2$ tide.

The lowest normal mode in the MAB sub-basin has a natural period of 6.70 h (NM3); this estimate is not significantly altered when the GOM sub-basin is included (NM4). The lowest MAB mode is concentrated around New York where the maximum amplitude occurs in the sharp corner formed by the coastline at $i = 40$. As indicated by the modal shape and phase shown in Fig. 3b, the mode crudely resembles a standing wave in the New York Apex. The small alongshore phase change over the region of significant modal amplitude indicates that the cross-shelf nodes of the mode propagate rapidly downcoast. This gives the appearance that the mode also is propagating downcoast.

We conclude that the lowest normal modes in the MAB sub-basin may be accurately determined without regard for the GOM, particularly those modes which are concentrated (like the lowest MAB mode) in the central and southern sections of the

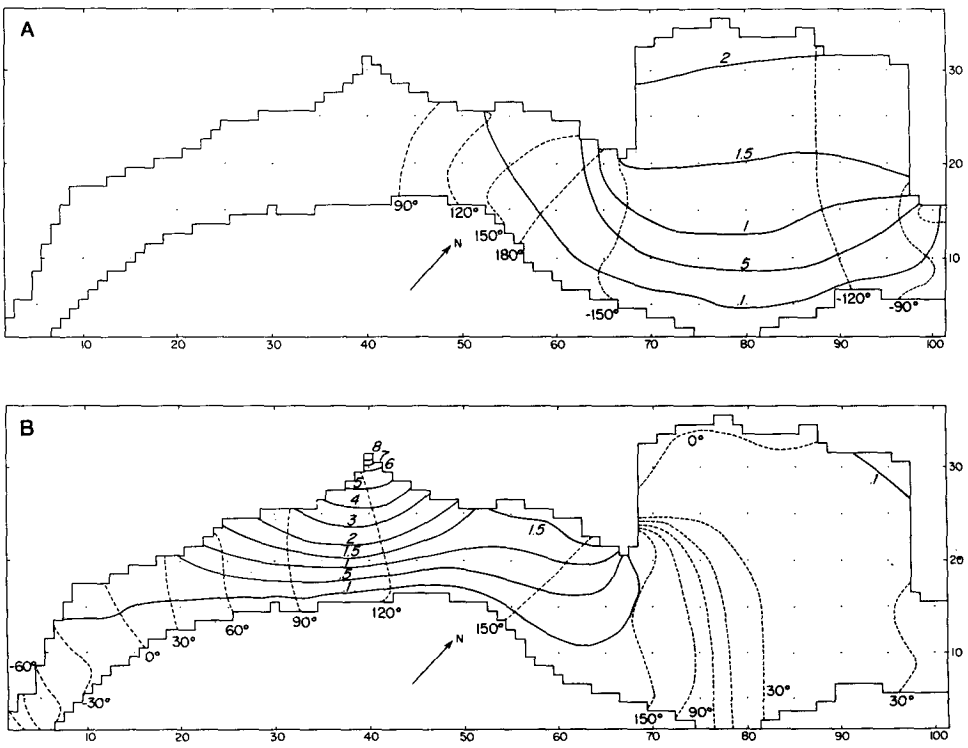


FIG. 3. Contour plots of modal amplitude and phase for the lowest GOM (A) and MAB (B) normal modes found in experiments NM2 and NM4, respectively.

MAB. This conclusion does not apply for some of the higher frequency modes of the whole model domain, particularly those modes which are concentrated near Nantucket. In contrast, the lowest normal mode in the GOM (without the Bay of Fundy) has a significant amplitude near Nantucket and is somewhat sensitive to the location of the southwestern boundary of the sub-basin. These results suggest that some part of the New England shelf—although perhaps not all of the MAB—should be included within the GOM domain in order to ensure accurate computation of its lowest normal modes.

## 4. Some free initial value experiments

To examine the free local wave response of the MAB model, we initialize the model at $t = 0$ with a non-equilibrium sea surface distribution. The initial velocity field is zero and no atmospheric forcing is applied. The model is then integrated for a period of 1–4 days and the surface elevation and current response examined. The initial shape of the surface elevation $\zeta$ is given by

$$\zeta_{ij}(t=0) = \begin{cases} 3(j_i - j_{0i}) \sin^2\left[\pi \dfrac{(i - i_{\min})}{(i_{\max} - i_{\min})}\right], \\ \qquad \text{for} \quad i_{\min} \leq i \leq i_{\max}, \\ 0, \quad \text{for} \quad i < i_{\min} \text{ and } i > i_{\max}, \end{cases} \tag{5}$$

where $j_{0i}$ is the value of $j$ (the $y$ index) at the shelf break at $i$. This expression represents a smooth mound of water located alongshore between $i_{\min}$ and $i_{\max}$ with an amplitude which increases linearly in $j$ from the open boundary at the edge of the shelf. In successive experiments, both the location of the center of the initial shape $i = (i_{\max} + i_{\min})/2$ and the alongshore extent $(i_{\max} - i_{\min})$ or effective wavelength have been varied. The parameters for the different experiments are shown in schematic fashion in Fig. 4. For brevity, we will discuss only a subset of these seven experiments.

The classic analyses of edge waves in a semi-infinite two-dimensional wedge by Reid (1958) and Kajiura (1958) suggest that the initial sea surface displacement should split into two mounds which propagate in both alongshore directions. Rotation causes the phase speed and the amplitude of the two mounds to differ, by amounts depending on the principal nondimensional parameter $\Gamma \equiv gsk/f^2$. The effect of rotation decreases as the alongshore wavelength ($k^{-1}$) decreases, i.e., as $\Gamma$ increases. With an effective cross-shelf slope of $s = 0.6 \times 10^{-3}$ in the New York Bight region, the value of $\Gamma$ in experiment IV1 is roughly 30, which is sufficiently large that good *qualitative* agreement is observed with Kajiura's analysis. The initial shape splits into two mounds of about equal amplitude moving upcoast and downcoast. The downcoast wave has a period of ~3 h observed at $i = 40$ (New York). This corresponds to a wavelength of ~100 km and a phase speed of 10 m s$^{-1}$ according to Reid's edge-wave dispersion curve. Quantitatively, agreement with the theoretical estimates is less good. The observed (simulated) wavelength is larger (150–250 km) as is the observed phase speed (18 m s$^{-1}$). As emphasized in Mysak's (1980) review of coastal-trapped waves, a finite depth at the coast, a variable

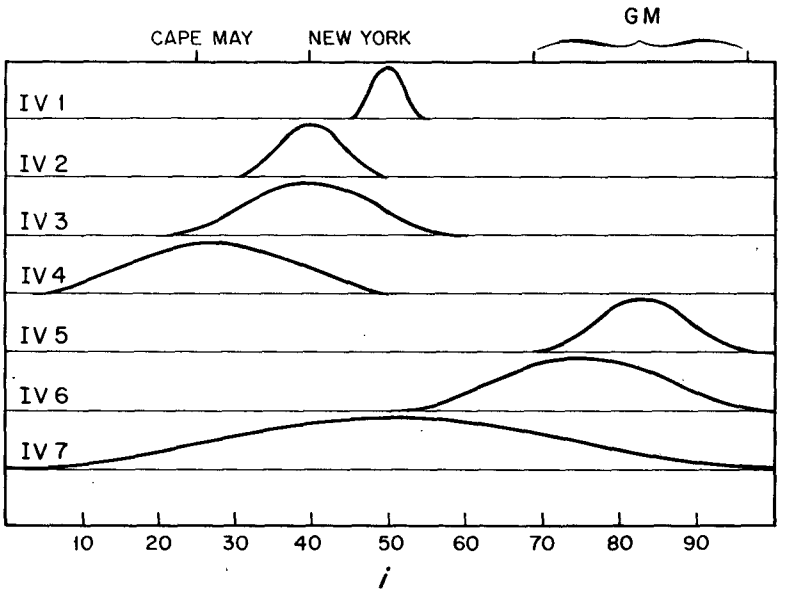


FIG. 4. A schematic diagram showing the alongshore structure of the initial $\zeta$ distribution used in the free initial values experiments IV1–IV7.

topography, and a curved coastline configuration all have strong effects on the propagation characteristics of edge and shelf waves. These factors mutually account for the differences between the computed results and the simple wedge model of Reid and Kajiura. Experiment IV1 does indicate, however, that short edge wave phenomena are supported within the MAB region of the numerical model.

The elevation shape used to initiate experiment IV2 closely approximates the shape of the lowest MAB normal mode so that that mode is clearly excited. The observed period at $i = 40$ equals $6.75 \pm 0.10$ h (based on 10 cycles) and little amplitude decrease occurs over the 4-day simulation. Due to weak quadratic bottom friction, the initial value experiments have a tendency for increased periods of the normal modes. The effective spindown timescale of the basin is large enough, however, that the periods of the damped and undamped modes do not differ greatly.

The alongshelf scale of $\zeta_0$ is doubled in experiment IV3. The initial response again agrees qualitatively with Kajiura's theory. The initial mound splits into two mounds which move up and down coast with approximate phase speeds of 160 and 120 km $h^{-1}$—some 60% faster than predicted, although the ratio of observed phase speeds (1.34) is close to the ratio of predicted phase speeds (1.44). The separating mounds leave a depression which begins to oscillate and exhibits the basic characteristics of the lowest MAB mode found in NM4. The resultant mode has a maximum amplitude at New York and a period of $6.80 \pm 0.11$ h based on 12 cycles, and the transition from positive to negative surface elevation propagates rapidly in the downcoast direction. Fig. 5

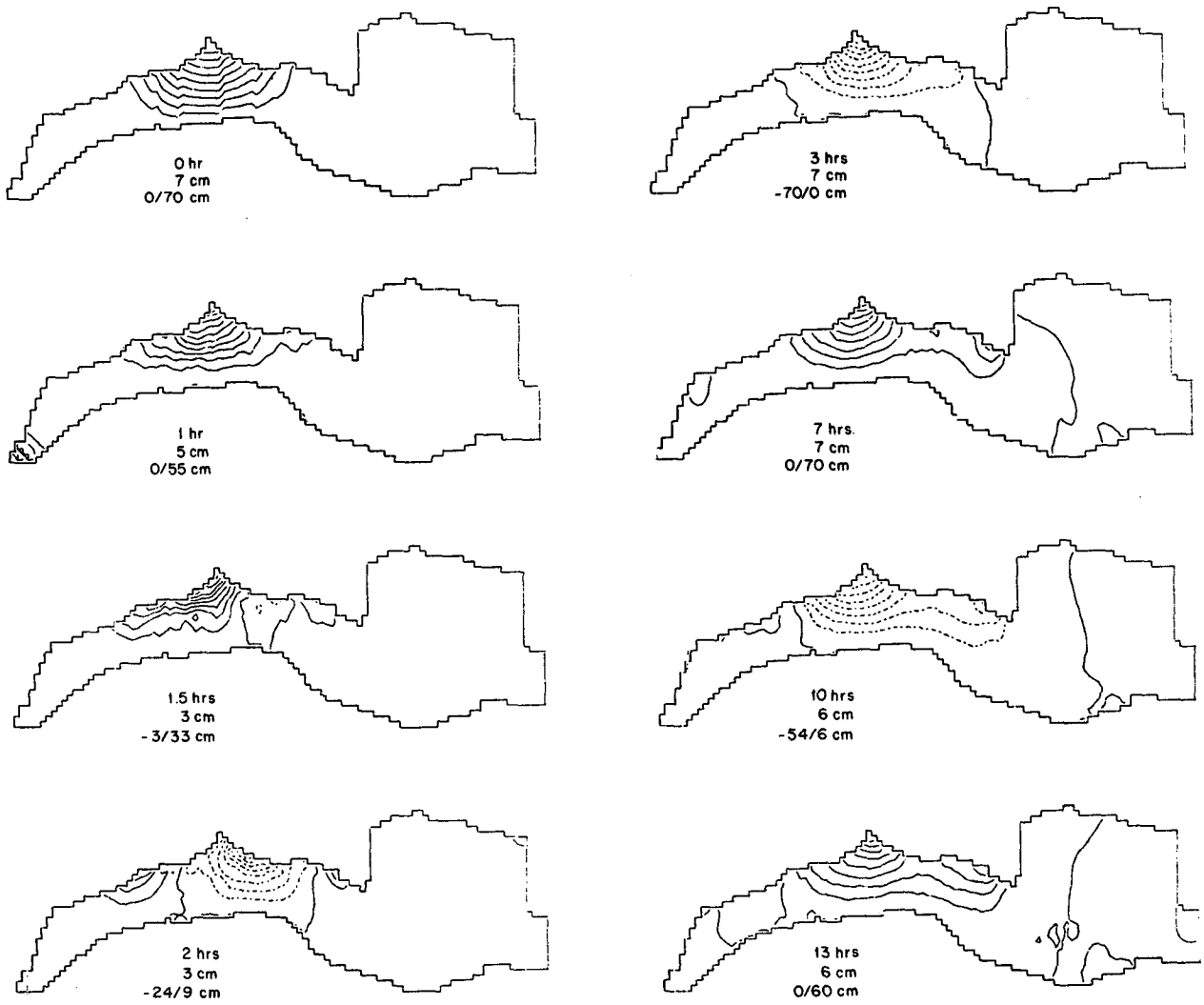


FIG. 5. Surface elevation maps at selected times showing the evolution of the surface elevation field in the initial value experiment IV3. The numbers inscribed under each plot give the time, contour level, and minimum/maximum contour value.

gives a sequence of sea surface elevation maps detailing the evolution of $\zeta$ in IV3.

Little energy leaks from the MAB into the GOM during experiments IV1 to IV4. The initial $\zeta_0$ distributions used in experiments IV5 and IV6 are centered in the GOM. In both experiments, the lowest GOM normal mode (found in NM2) is excited. The observed natural periods are 10.2 ± 0.4 h in IV5 and 10.3 ± 0.4 h in IV6. Other higher gravitational modes also are excited, both in the GOM (in IV5 and IV6) and over the New England shelf (in IV6). The coastal sea surface elevation field at New York ($i = 40$) exhibits a small but pronounced 4.0 ± 0.1 h oscillation, indicating that the lowest MAB mode is not excited to any noticeable extent.

In summary, these free initial value experiments demonstrate that short shore-trapped mounds (or depressions) of water behave like edge waves in the model MAB. The longer shore-trapped mounds excite the lower normal modes of the basin in both the MAB and GOM. Within the MAB, these modes have maximum surface elevation amplitudes at the coast and have an apparent downcoast phase propagation.

## 5. Impulsive uniform stress experiments

We have conducted several initial value experiments in which a spatially uniform wind stress is applied at $t = 0$ to the initially quiescent fluid. The stress is held constant in space and time for the duration of the simulations which typically last four days. The intent here is to examine the time scales with which the MAB adjusts to sudden changes in wind stress. In separate experiments, both the magnitude and direction of the wind-stress vector and the bottom-drag coefficient have been varied to study the general wind-driven transient behavior of the model and the influence of the nonlinear bottom-stress law.

Two initial experiments clearly show that the model response is strongly dependent on the orientation of the wind-stress vector and the geometry of the nearcoast region. Consider first an alongshelf surface stress of 2 dyn cm$^{-2}$ applied in the negative (downcoast) $x$ direction. The resulting values of coastal sea level, surface elevation, and alongshore transport are shown as a function of time in Figs. 6, 7, and 8 respectively. These figures indicate that the transient wind-driven response within the MAB and GOM sub-basins differ significantly, directly reflecting the difference between the relatively simple and smooth shelf topography within the MAB and the deeper and more complex topography within the GOM.

The transient response within the MAB to an alongshore wind stress is dominated by the effects of friction and rotation. The downcoast wind begins to drive downcoast currents which tend to follow the regional bathymetry and coastline. The surface elevation field sets up against the coast in crude geostrophic balance with the alongshore flow; as the alongshore currents intensify with time, the quadratic bottom stress becomes more important in the momentum balance (Fig. 9). However, except in the most shallow MAB regions, the cross-shelf sea surface slope and alongcoast velocity component are in approximate geostrophic balance. A transient oscillation with a period of ~6 h (Fig. 6) excited by the sudden turn-on of the wind stress are quickly dissipated within 1–2 days as the flow and elevation fields within the MAB approach an equilibrium steady-state solution. Frictional damping is particularly enhanced in the shallower southern section of the MAB, causing the very rapid dissipation of the higher frequency transient motions occurring there (Figs. 6 and 9a). In the deeper northern section of the model, the initial surface elevation adjustment occurs more rapidly but less effective local damping allows some overshoot and a longer time is required for the transient motions to disappear.

Thus several time scales appear to be important in the regional adjustment process: a local frictional

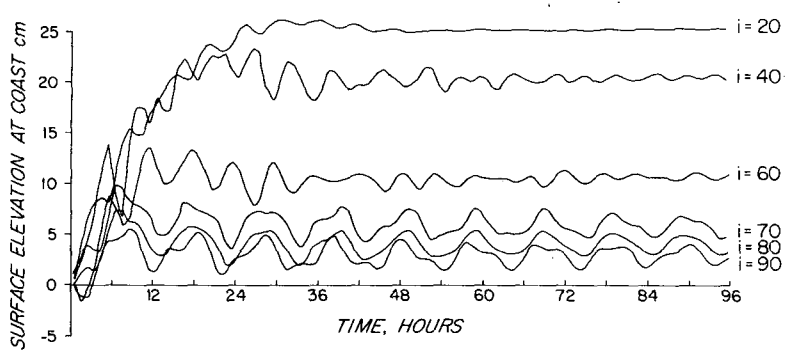


FIG. 6. Time history of surface elevation at selected coastal positions when a steady stress of 2 dyn cm$^{-2}$ has been applied in the negative (downcoast) $x$-direction at $t = 0$.

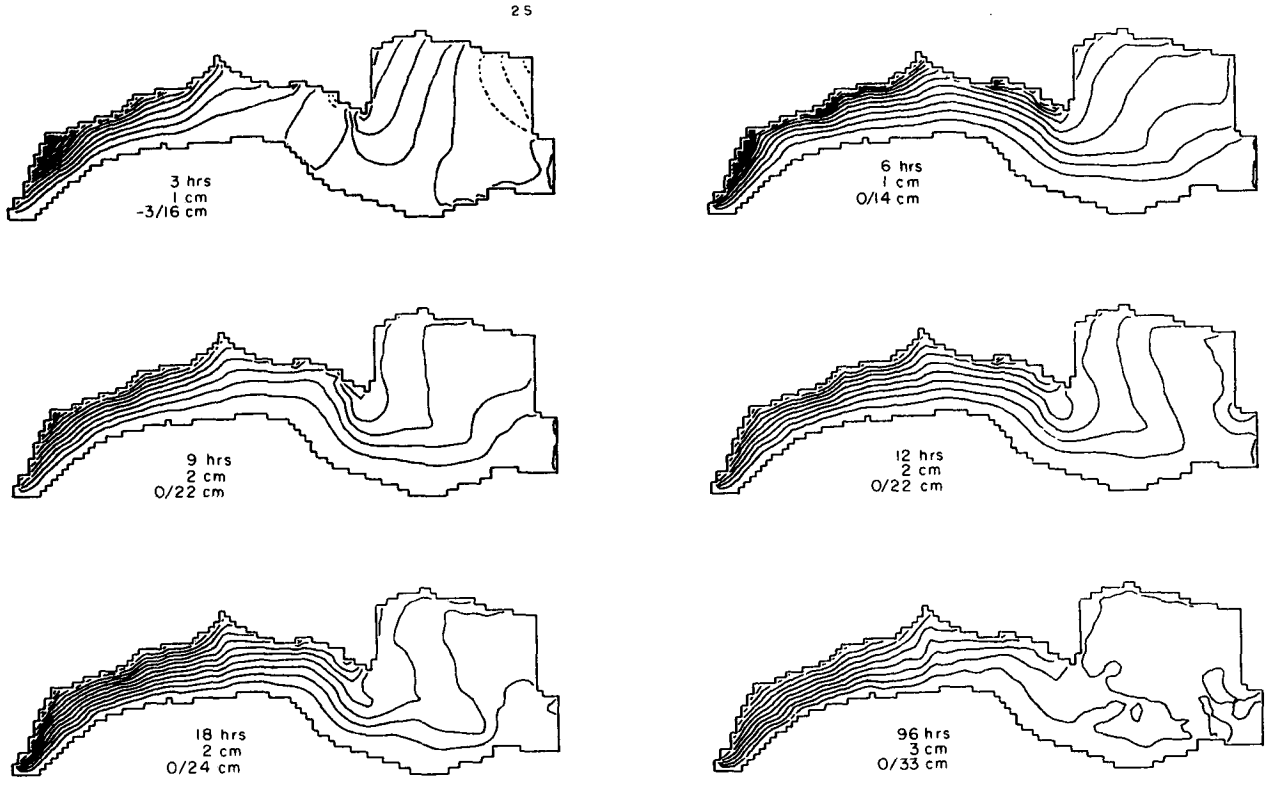


FIG. 7. Surface elevation (or equivalent SSP) contour maps at $t = 3, 6, 9, 12, 18$ and 96 h after a steady 2 dyn cm$^{-2}$ wind stress has been applied in the negative (downcoast) $x$ direction at $t = 0$.

time scale dependent on the strength of the depth-averaged velocity field, an inertial time scale dependent on the regional long-wave propagation speed, and a longer time scale which reflects the adjustment process within the entire model domain. An approximate estimate of this longer time scale can be made by fitting a simple exponential function to the alongshore transport curve shown in Fig. 8.

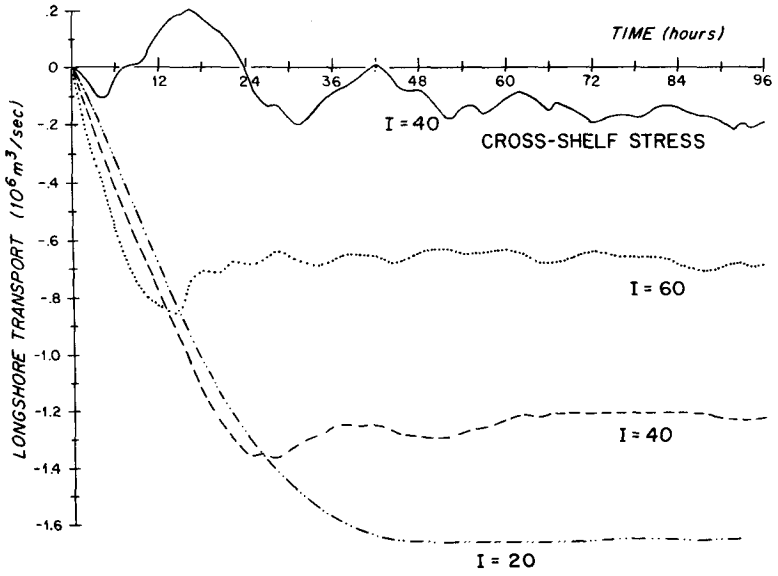


FIG. 8. Time history of total alongshore transport through cross-shelf sections at $i = 20$, 40 and 60 driven by impulsive alongshore forcing ($\tau_x = -2$ dyn cm$^{-2}$, $\tau_y = 0$) and at $i = 40$ driven by impulsive offshore forcing ($\tau_x = 0, \tau_y = -2$ dyn cm$^{-2}$).

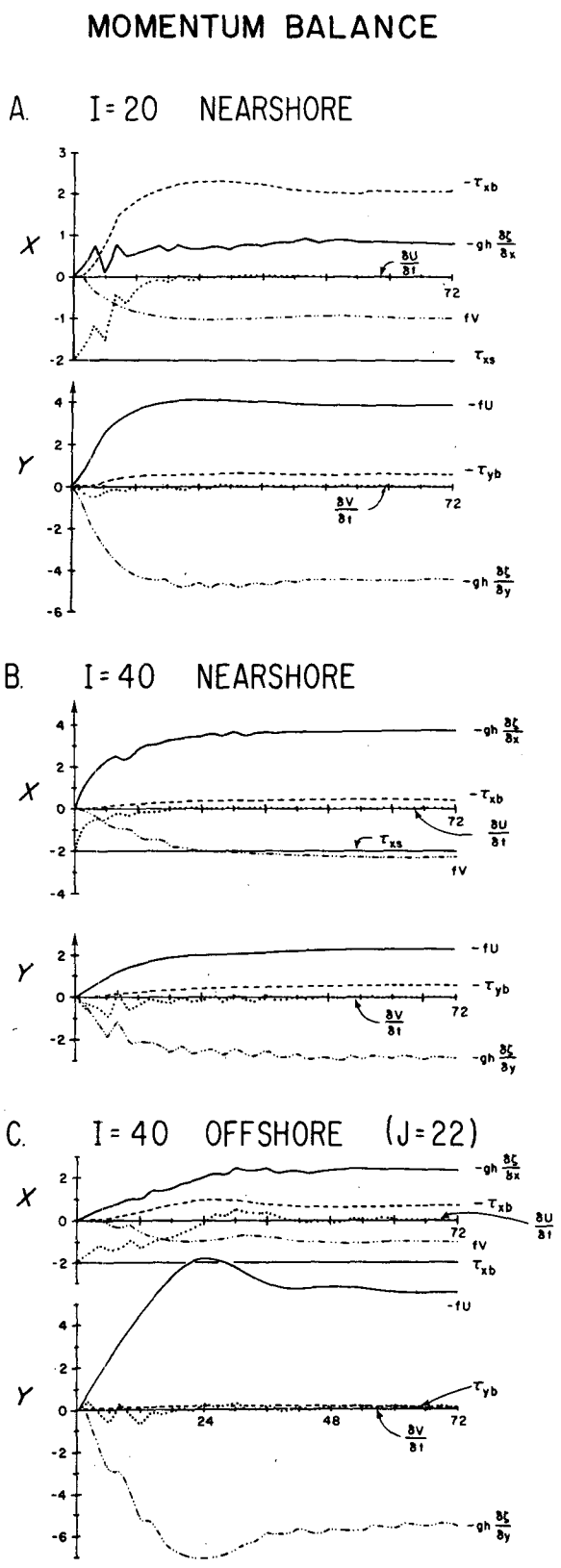


Spinup of the MAB to a 2 dyn cm$^{-2}$ alongshore wind stress is thus crudely characterized by an $e$-folding adjustment time which varies geographically from ~12 h in the southern MAB ($i$ = 20), to 10 h at New York ($i$ = 40), to 4 h at Nantucket ($i$ = 60). Since the decay time $\tau_d$ should decrease with increasing alongshore wind stress (due to the quadratic bottom stress), we note here that the effective decay time for the MAB is sufficiently short in comparison to the 2–10 day time scales characterizing storms that wind-driven transient motion should be quasi-steady. This question will be examined in more detail in the next section.

The degree to which geostrophy holds between the steady-state distributions of sea surface elevation and velocity in the MAB can be seen in Fig. 10, in which are plotted the steady-state (i.e., $t$ = 96 h) $u$-component and $v$-component momentum balances along transects taken at $i$ = 20, 40 and 60. Note the near geostrophic character of the alongshelf transport component along the three transects plotted. Even in the shallowest regions (southern MAB, $i$ = 20), bottom stress contributes roughly only 10% to the momentum balance in the cross-shelf direction.

Along some cross-shelf transects, the structure of the surface elevation and longshore current fields is particularly simple. Fig. 11 shows the time evolution of these fields along $i$ = 45. Note the nearly linear decrease in $\zeta$ from its maximum value attained at the shore to zero at the shelf break. In addition, the $u$ velocity component is nearly constant. The nearly linear $\zeta$ setup and approximately constant $u$ distributions obtain throughout the time history of this experiment. The approximately constant cross-shelf elevation slope and geostrophic balance implies that the alongshelf transport $T = g(A/f)\zeta_c$, where A is the cross-shelf area and $\zeta_c$ is the coastal sea level elevation.

For the downcoast wind stress, the initial surface elevation adjustment occurs very rapidly (within several hours) within the GOM, but the relatively large mean depth of this sub-basin effectively prevents much frictional damping of the resulting currents. The surface elevation field clearly overshoots its equilibrium pattern and a ringing of the slightly-damped normal modes occurs. Spectral analysis of the coastal surface elevation data for the GOM shown in Fig. 6 and the elevation contour maps of Fig. 7 indicate that the most energetic mode excited is in fact the 10.7 h lowest GOM mode found in experiment NM2. The next most energetic mode has a period of 4.8 ± 0.1 h and an amplitude half that of the lowest mode.

FIG. 9. Time history of terms in the $x$ and $y$ momentum balances at selected points in the MAB: (A) $i$ = 20 (nearshore), (B) $i$ = 40 (nearshore), (C) $i$ = 40 (mid-shelf). Units = 1 cm$^2$ s$^{-1}$.

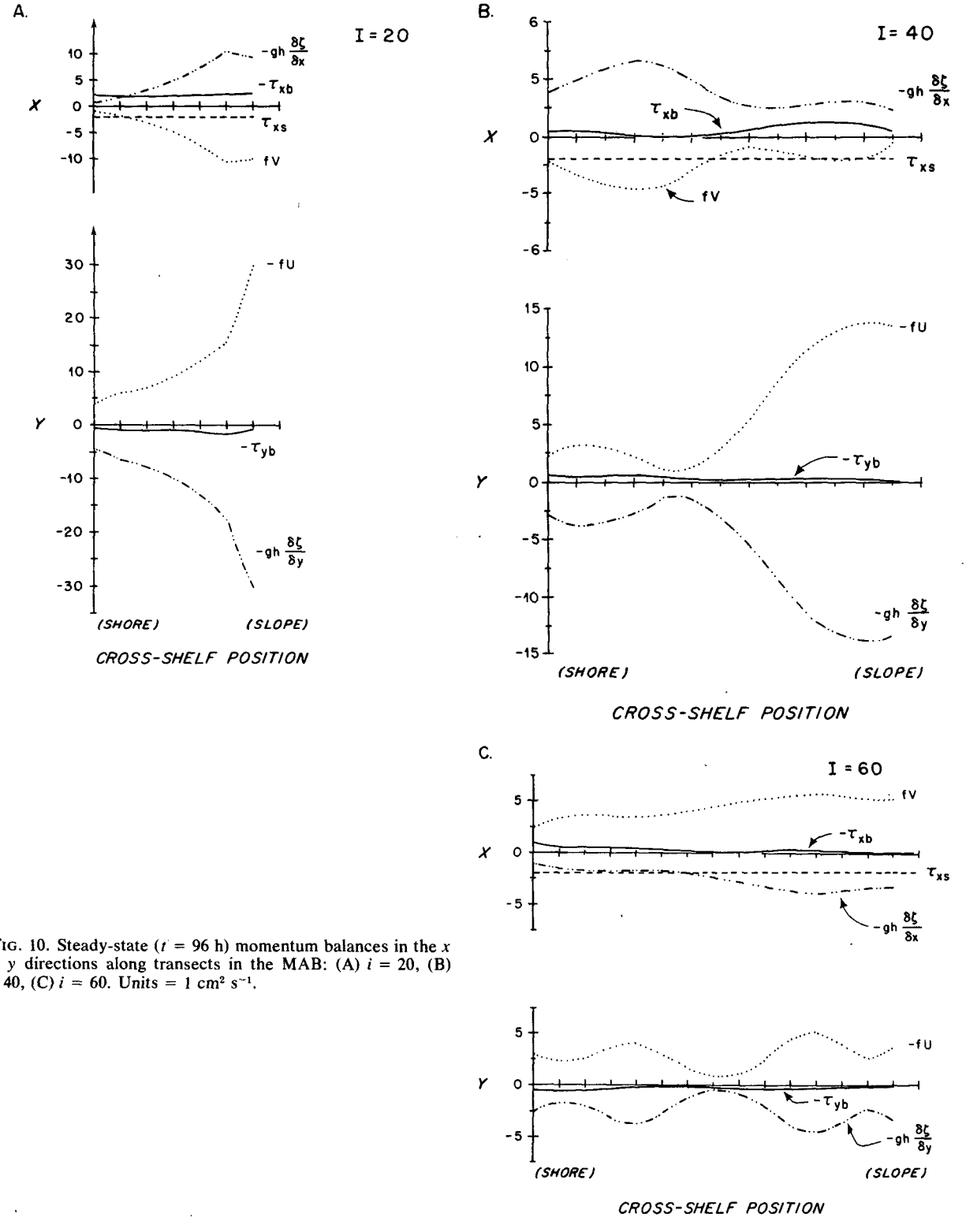


FIG. 10. Steady-state ($t$ = 96 h) momentum balances in the $x$ and $y$ directions along transects in the MAB: (A) $i$ = 20, (B) $i$ = 40, (C) $i$ = 60. Units = 1 cm$^2$ s$^{-1}$.

Even though these modes remain energetic throughout the 4-day experiment, several features of the equilibrium surface elevation pattern within the GOM can be seen in Figs. 6 and 7. Unlike the rather simple, monotonic surface elevation pattern found within the MAB, the elevation pattern within the GOM is complicated by a small surface setup over Georges Bank, again in crude geostrophic balance

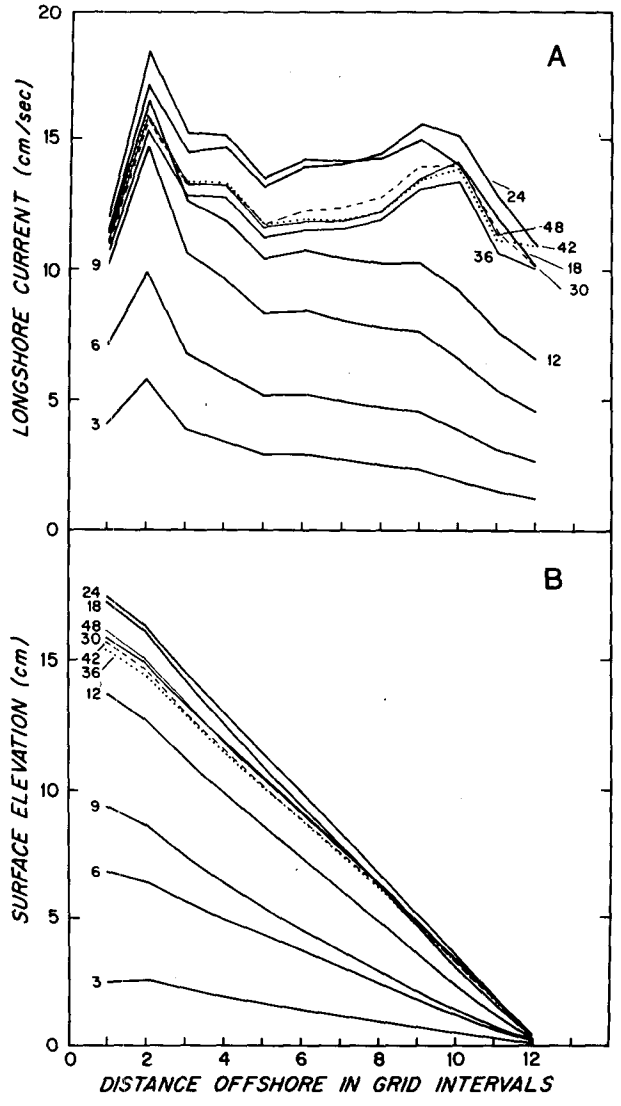


FIG. 11. The time evolution of the cross-shelf structure of the $x$-velocity component (A) and surface elevation (B) at $i = 45$.

with a strong clockwise flow around the northern edge of Georges Bank and directed downcoast along the southern side of Georges Bank into the MAB. Frictional damping is significant over the very shallow Nantucket Shoals and southern Georges Bank region; as a result, the elevation and transport response there rapidly approaches a steady state. (Thus the southern flank of Georges Bank may be considered an extension of the MAB in both a geographical and dynamical sense.) The equilibrium surface elevation response within the deeper GOM (to the northwest of Georges Bank) is a downwind setup of ~4.5 cm, approximately consistent with the dynamical balance $\tau_x = gh\zeta_x$ for a narrow enclosed basin 350 km long and 150 m deep. A narrow zone of coastal setup to the right of the wind stress also occurs along the western boundary of the GOM, causing the surface elevation contours to bend around the western corner of the GOM (see Fig. 7).

The initial current response within the GOM is downcoast along both the southern flank of Georges Bank and the northwestern boundary of the GOM, causing both downwind setup and an upwind return flow through the deeper mid-section of the GOM. The basic features of this initial response were correctly predicted by Csanady (1974) who considered the barotropic response of a simpler, more idealized GOM (cf. Csanady's Fig. 9 with our Fig. 7). The strongest return flow occurs along the northern side of Georges Bank and out through the Northeast Channel, where the depth-averaged currents reach a peak speed of 37 cm $s^{-1}$ at $t = 48$ h. This transport field becomes more complex with increasing time as smaller gyres develop over the rough topography within the GOM and the flow through the Northeast Channel diminishes in strength. The experiment was too short to determine the equilibrium transport pattern.

For comparison, consider the transient response to an *offshore* windstress of magnitude 2 dyn $cm^{-2}$. With the wind directed in the negative $y$ direction, the resulting coastal sea level, surface elevation, and alongshore transport behavior are shown in Figs. 12, 13 and 8, respectively. The transient response in this case is more complex, and the wind-driven currents are sufficiently weak over most of the model domain that a frictional steady state balance is not achieved by the end of the 4-day experiment. The exception to this statement occurs along the southernmost coast (for $i \leq 20$) where the applied wind stress has a component parallel to the local coastline. In this very shallow area, the steady local coastal setup shown in Fig. 12 accompanies relatively strong downcoast flow. This region of mean downcoast flow extends upcoast to $i = 40$ although the alongshore transport there is quite weak as shown in Fig. 8.

A mean setdown occurs over the rest of the model, with a maximum coastal setdown of 12 cm occurring at New York ($i = 40$) and a mean setdown of 3.5 cm along the northwestern edge of the GOM. A significant alongshore surface elevation gradient is thus created in the southern MAB, in opposition to the alongshore flow. A significant alongshore elevation gradient also exists over the New England shelf. Within the central MAB, near $i = 40$, a crude geostrophic balance between alongshore flow and cross-shelf surface elevation gradient does not exist.

The high-frequency oscillatory motions excited by the sudden turning on of the wind stress persist without significant damping throughout this experiment. The quadratic bottom-stress law implies that the local frictional damping rate be proportional to the

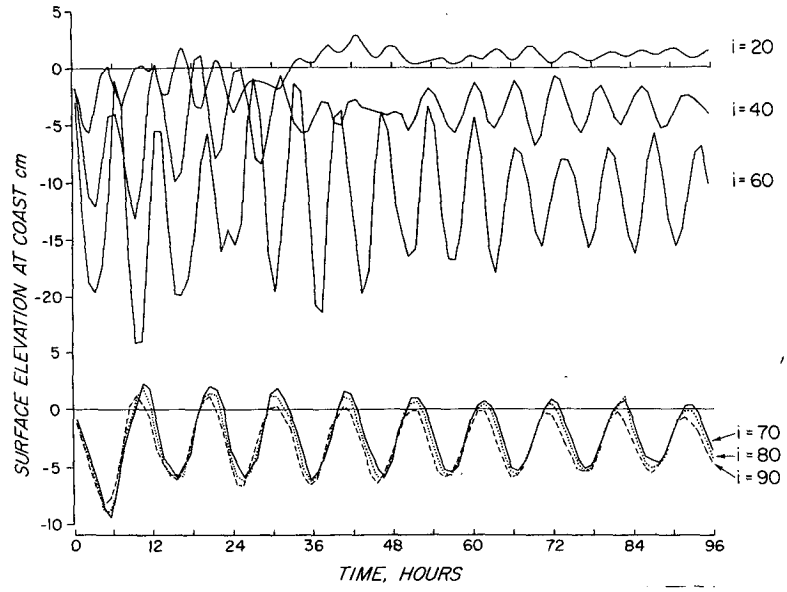


FIG. 12. Time history of surface elevation at selected coastal positions when a 2 dyn $cm^{-2}$ wind stress is applied in the negative (offshore) $y$ direction at $t = 0$.

magnitude of the local transport. Since the offshore wind drives only very weak alongshore transports over most of the model, the effective damping rate is quite small. Spectral analysis of coastal sea level confirms the visual impression given by Figs. 12 and 13 that the lowest MAB and GOM normal modes discussed in Section 3 are the two principal modes excited by an offshore wind.

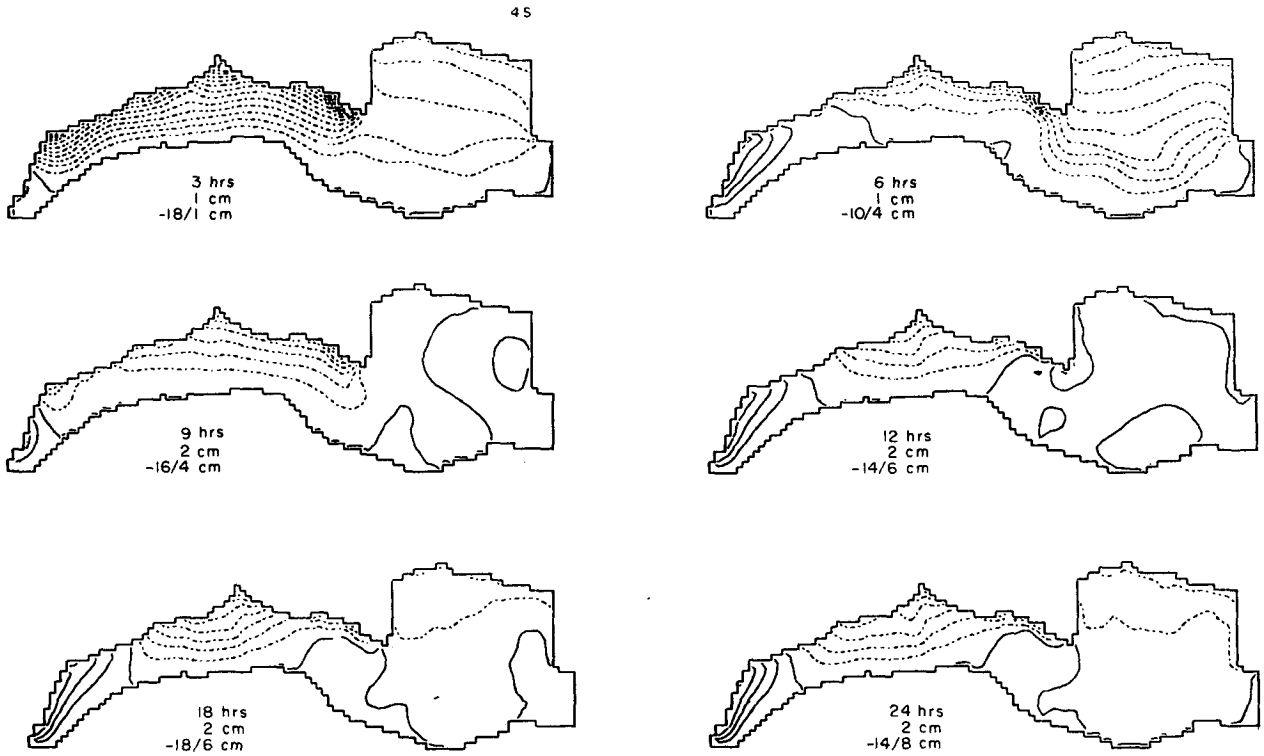


FIG. 13. Surface elevation contour maps at $t = 3, 6, 9, 12, 18$ and 24 h after a steady 2 dyn $cm^{-2}$ wind stress is applied in the negative (offshore) $y$ direction.

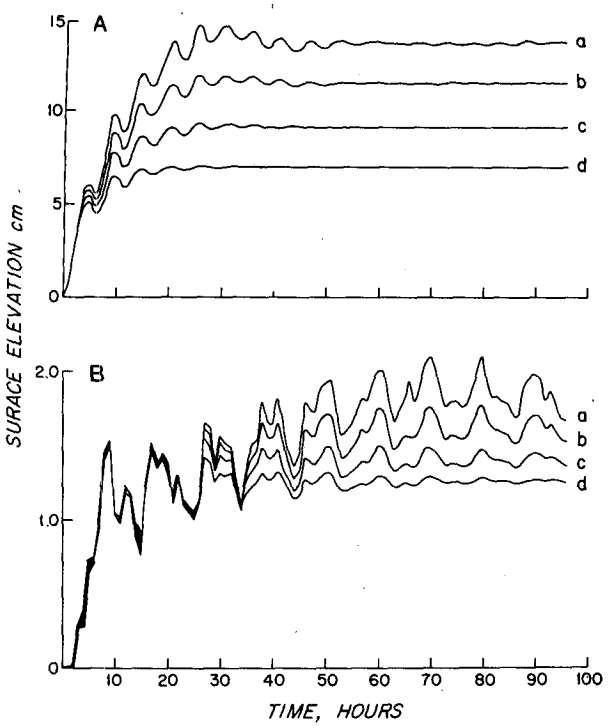


FIG. 14. Surface elevation at coast at $i = 25$ in (A) and surface elevation on Georges Bank at $i = 75, j = 15$ in (B) versus time. The product of $10^2 C_D \tau_x$ for the different lettered curves is (a) 0.5, (b) 1.0, (c) 2.0, and (d) 4.0.

As shown in Fig. 12, oscillations in coastal sea surface elevation along the northern boundary of the GOM are in phase and of approximately equal amplitude, consistent with the structure of the lowest GOM mode shown in Fig. 3a. Although little frictional retardation of the modal oscillation occurs during the 4-day experiment, the mean set down within the GOM appears to be ~3.5 cm. Most of the variation in $\zeta$ occurs in the offshore direction; little differential setup is maintained in the $x$ direction across the GOM.

These two numerical experiments demonstrate that model flows driven by alongshore winds reach a frictional steady-state rather quickly within the MAB and over the southern side of Georges Bank. The steady-state that is achieved, of course, must depend on the applied alongshore wind stress $\tau_x$ and the frictional parameters. However, it is clear from the model momentum Eqs. (1) that the volume transport and surface elevation variables scale proportionally to $\tau_x$ provided the product $(C_D \tau_x)$ is constant. Thus the response scaled by $\tau_x$ for $\tau_x = 2$ dyn cm$^{-2}$ with $C_D = 0.0025$ is identical to the scaled response for $\tau_x = 1$ dyn cm$^{-2}$ with $C_D = 0.005$.

Time series of sea surface elevation are shown in Fig. 14 for four values of the controlling parameter $(C_D \tau_x)$ equaling 0.005, 0.01, 0.02, and 0.04. Fig. 14a shows the variation in transient response for coastal $\zeta$ at $i = 25$ (in the southern MAB). Although the initial ($t \leq 4$ h) adjustment of coastal sea level appears to be insensitive to the value of $(C_D \tau_x)$, equilibrium values of $\zeta_c$ ($i = 25$) are clearly dependent in the expected systematic fashion on this product. As $(C_D \tau_x)$ increases, frictional processes are increased in strength, resulting in decreased steady-state values of coastal sea surface displacement. Note also that transient oscillations in $\zeta_c$ persist out to $t = 4$ days where the lowest values of $(C_D \tau_x)$ are used. A similar behavior is also seen in Fig. 14b in the sea level response recorded over Georges Bank at $i = 75$, $j = 15$. In this location, however, the initial adjustment of sea level is nearly independent of $(C_D \tau_x)$ for $t \leq 24$ h, reflecting the relative insensitivity of the lower GOM modes to bottom friction.

The scaled *steady-state* coastal sea level and alongshelf transport obtained in these experiments are plotted in Fig. 15 as a function of alongshelf position. Fig. 15a indicates that a mean alongshore elevation gradient is set up in the MAB in opposition to the applied along-shelf wind stress. The amplitude

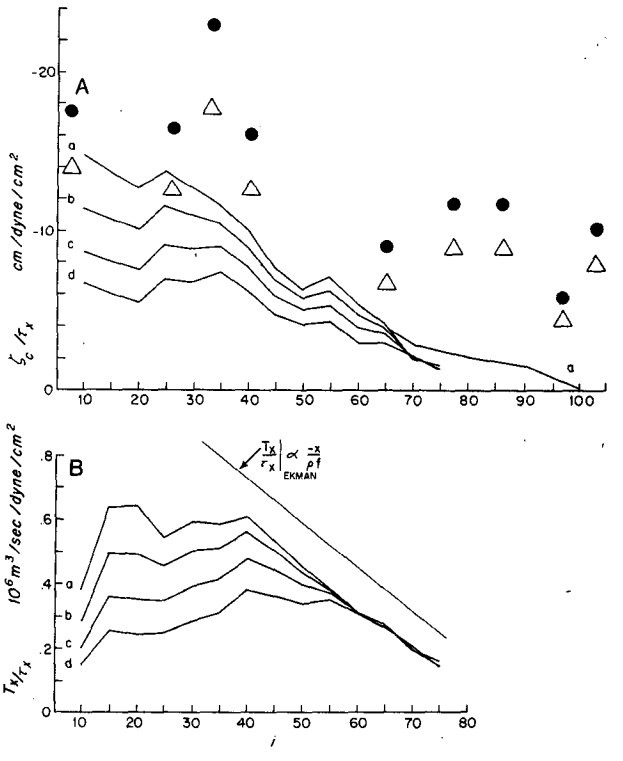


FIG. 15. Quasi-equilibrium values of coastal sea level (A) and alongshore transport (B) scaled by $\tau_x$ plotted as a function of the alongshore coordinate $i$. Product of $10^2 C_D \tau_x$ for different lettered curves is (a) 0.5, (b) 1.0, (c) 2.0, and (d) 4.0. Sloping line in (B) is relative alongshore transport predicted by Ekman transport model. Observed (●) and adjusted (△) coastal response for a nominal 1 dyn cm$^{-2}$ alongshore wind stress for various locations are also shown.

of the alongshore gradient clearly increases with an increase in $\tau_x$ or $C_D$, although the quadratic drag law reduces the proportional increase, especially in the southern half of the MAB where we found the most pronounced frictional damping of the high-frequency transient modes. The irregular coastline near $i = 25$ and $i = 55$ cause local coastal sea level maxima, making the alongshore coastal elevation pattern non-monotonic. This effect seems confined to narrow nearshore zones so that the alongshore elevation pattern appears monotonic over the mid- and outer shelf.

As the effective frictional damping is increased by either increasing $\tau_x$ or $C_D$, the alongshelf transport within the MAB reaches a maximum amplitude near $i = 40$. As shown in Fig. 15b, the effect of nonlinear damping is most clear in the southern section of the MAB, where for moderate values of $\tau_x$ and $C_D$, the alongshore transport does not vary much over the 400 km long section of shelf between $i = 15$ and $i = 40$–$50$. This response is in sharp contrast with the essentially *linear* response of coastal sea level and alongshelf transport over the New England shelf and southern Georges Bank section between $i = 55$ and 75. The average slope of the alongshelf transport observed there is close to the prediction $\partial/\partial x(T_x) = -\tau_x/\rho f$ based on a steady-state surface Ekman layer.

## 6. Translating storm experiments

In the preceding impulsive stress experiments, the effective frictional decay time for the MAB appears to be roughly O(10 h). This suggests that the response in the MAB to evolving wind stress patterns should be quasi-steady for stresses which change more slowly in time. We have tested this possibility for a localized, translating distribution of atmospheric pressure and surface wind stress, designed to represent an idealized strong cyclonic storm.

The model storm is elliptical in shape with half-axis lengths of 700 and 560 km, respectively. The atmospheric pressure deviation ($\zeta_a$) varies smoothly from 10 cm at the storm center to zero at the storm edge. The accompanying surface wind stress is computed using the quadratic stress law $\boldsymbol{\tau}_s = \rho_a C_D |\mathbf{w}_{10}| \mathbf{w}_{10}$, where $\mathbf{w}_{10}$ is the wind velocity at 10 m, $\rho_a$ is the density of air and $C_D = 0.0015$. Values of $\mathbf{w}_{10}$ are obtained by 1) computing the geostrophic surface wind from the assumed atmospheric pressure pattern, 2) applying the gradient wind correction to account for the centrifugal effect of isobaric curvature, and 3) rotating the resulting corrected geostrophic velocities by an (assumed constant) ingress angle of 15° and reducing their magnitude by 30% (Hasse, 1974). Fig. 16 shows the wind speed and wind stress distributions.

Two moving storm experiments will be described. In each experiment the idealized storm pattern is moved in the upcoast direction at a constant speed of 10 m $s^{-1}$. The two straight storm tracks in Fig. 17 lie to the south and north of the model domain. In both experiments the storm passes over the model domain in about two days.

The time evolution of the surface elevation field is shown in Fig. 18 for experiment MS-1. The storm

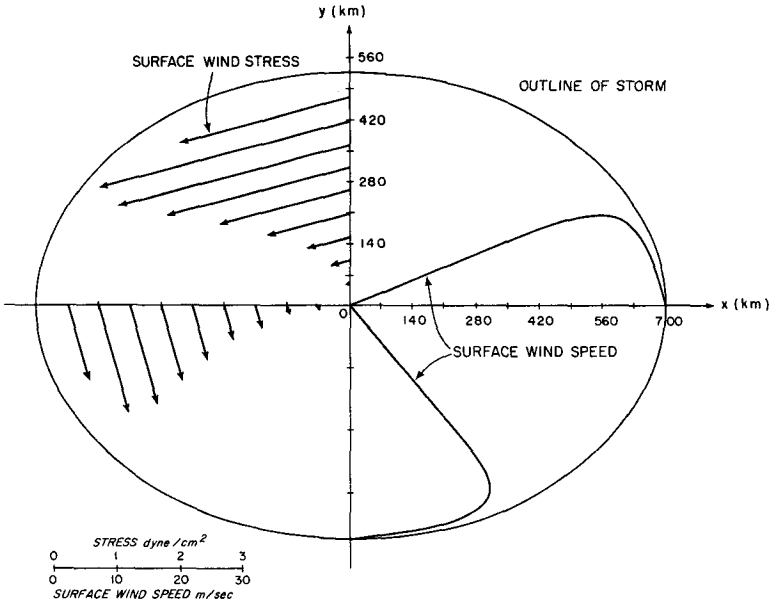


FIG. 16. The spatial structure of the idealized storm used in the moving storm experiments.

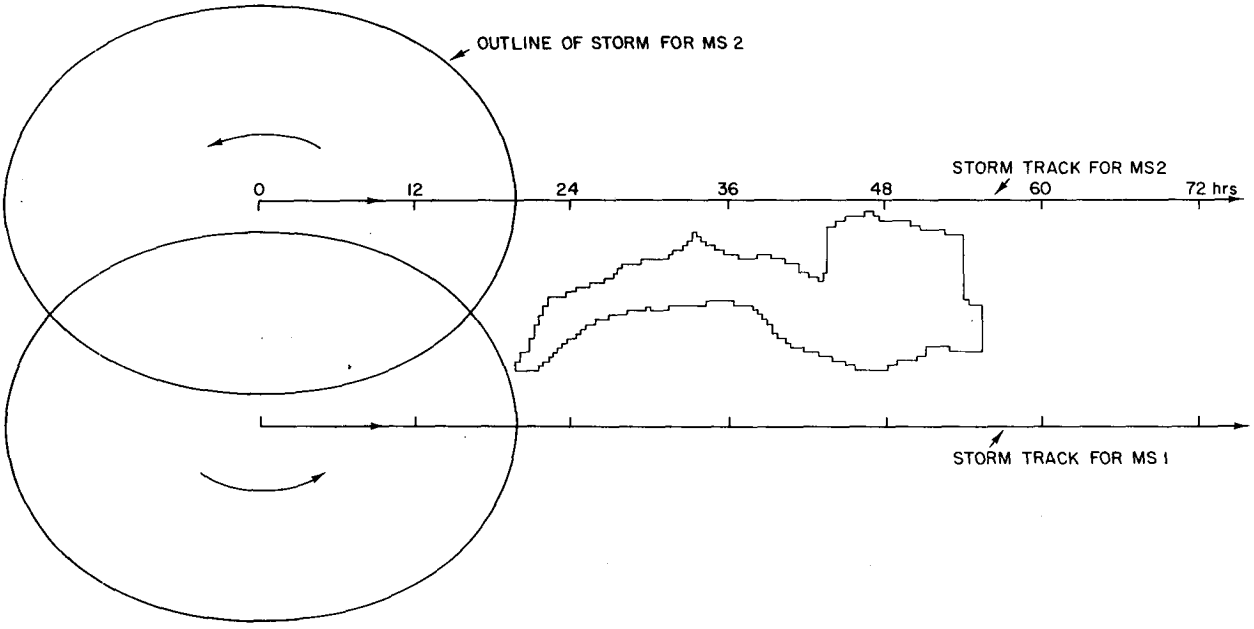


FIG. 17. Schematic of storm tracks used in the two moving storm experiments MS1 and MS2.

trajectory lies south of the model in this experiment and as a result, the storm causes a strong downcoast wind stress over much of the MAB. As the storm moves into the MAB, therefore, strong setup of sea level occurs in the Southern section, as was observed in the impulsive downcoast-directed wind-stress experiments. Accompanying the setup are strong alongshore gradients of $\zeta$ which persist recognizably for ~24 h after the direct influence of the moving storm has subsided. Coastal sea level fluctuations south of New York tend to propagate downcoast (southward) after the storm has passed. Within the GOM, systematic sea level slopes are briefly established during the passage of the storm offshore; however, these regional sea level slopes rapidly break down into a series of transient smaller scale oscillations after the storm has left the model domain.

Within the MAB, surface elevation and alongshore transport are in approximate geostrophic balance. We recall from Section 5 that since $\zeta$ and $u$ have nearly linear and constant distributions at some cross-shelf locations, a unique local steady-state relationship appears to exist between coastal sea surface elevation and total alongshore transport at these sites. We have used this approximate proportionality factor to predict at $i = 45$ the alongshore transport in MS-1 on the basis of the adjusted surface elevation observed in MS-1. The comparison between this prediction and the observed model transport is shown in Fig. 19. The transport predictions are low by ~10–20%, although the shapes of the two transport curves are similar. These results clearly suggest that the passage of the moving storm in this experiment is sufficiently slow relative to the adjustment time within the MAB that the response there is quasi-steady. Note finally that the time lag between the maximum alongshore wind stress and the maximum coastal sea surface elevation and alongshore transport is ~12 h.

The surface elevation and transport patterns observed within the model MAB, of course, are dependent on the particular storm track followed. In the second moving storm experiment, MS-2, the storm center moves along the northern side of the model domain so that the wind-stress field has a strong onshore/offshore component and a smaller upcoast component. As shown in Fig. 20, the resulting surface elevation is strongly set down in the MAB with persistent gradients in $\zeta$ of opposite sign, but of comparable magnitude, to those observed in MS-1. Within the MAB the surface elevation response is dominated to large degree by the onshore/offshore wind-stress component.

The onshore component in the leading edge of the storm causes an initial sea level rise along the coast which is then followed by strong setdown during the latter half of the storm and later. Using the same proportionality factor between coastal sea level and alongshore transport used in MS-1, we have predicted the total alongshore transport using the model values of coastal adjusted surface elevation. The comparison between this prediction and the model total alongshore transport is shown in Fig. 21. While crude agreement is observed after about $t = 60$ h, the initial behavior is quite different. The

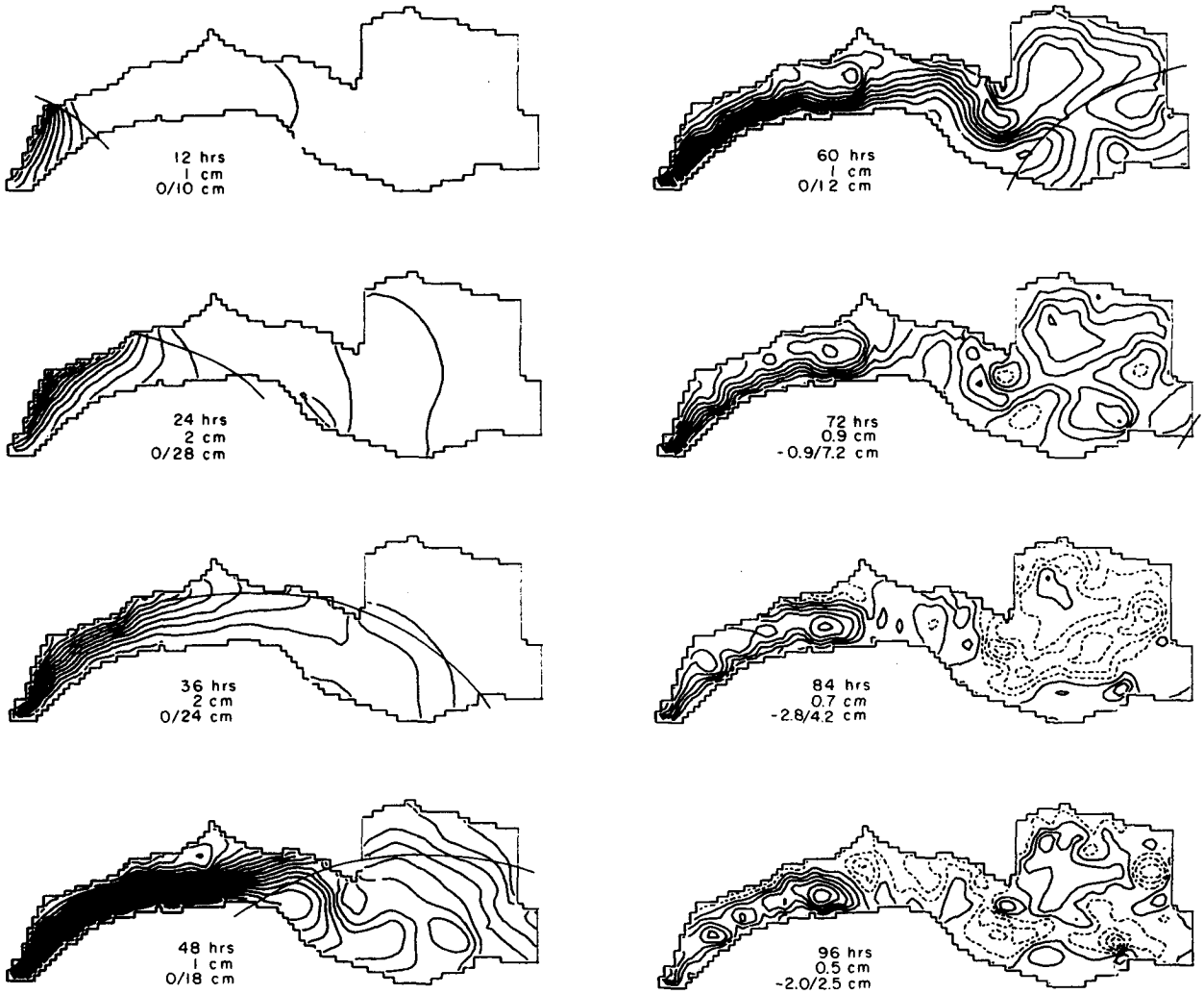


FIG. 18. Surface elevation contour maps at 12 h intervals during experiment MS1. (In this figure atmospheric pressure fluctuation has not been added to the surface elevation field.) The outline of the storm is also shown.

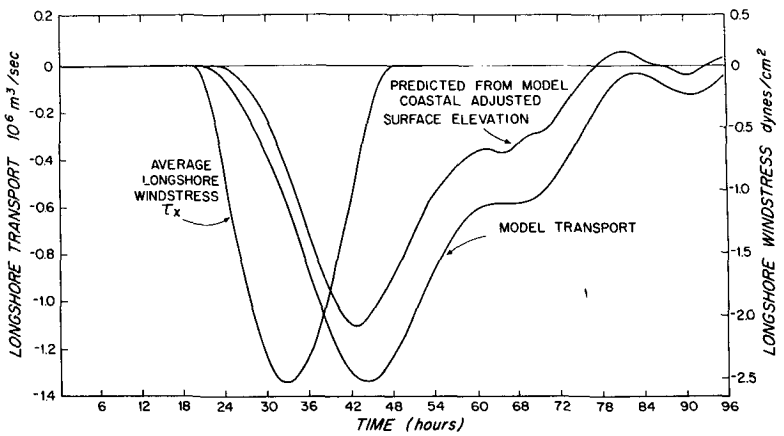


FIG. 19. Time history of the alongshore wind stress, the model total alongshore transport, and the alongshore transport predicted from the model coastal adjusted surface elevation at $i = 45$ in experiment MS1.

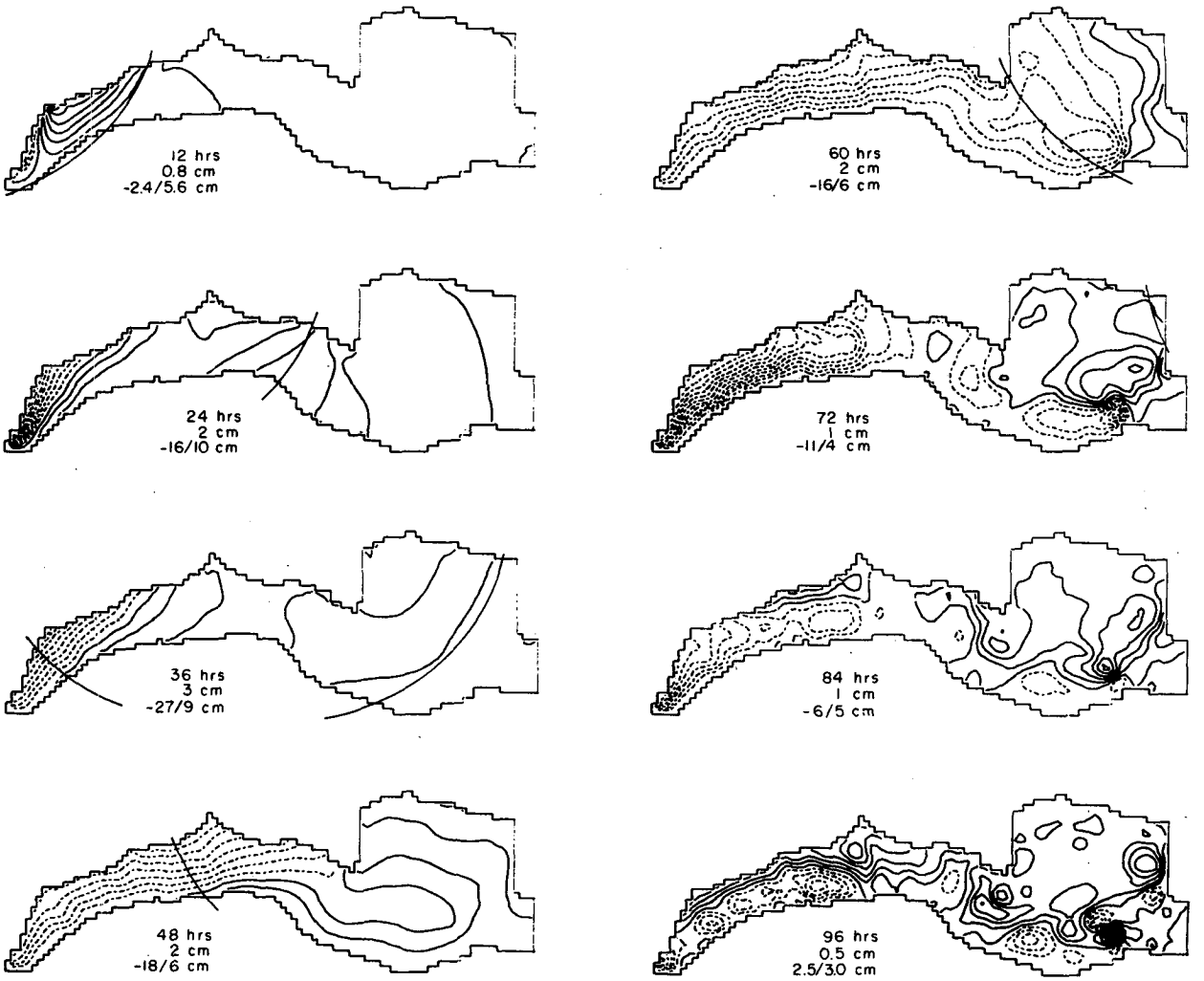


FIG. 20. Surface elevation, contour maps at 12 h intervals during experiment MS2. The storm outline also is shown for reference.

observed transport is upcoast while the predicted transport is initially downcoast between $t = 16$ and 30 h due to the initial setup caused by the leading edge of the storm. This difference is presumably due in part to the longer time required for the model to adjust to an offshore wind stress (see Section 5). Even so, the maximum coastal adjusted surface elevation and transport lag the wind-stress maximum by some 4–8 h. South of New York, coastal sea level fluctuations tend to propagate downcoast after the storm has passed. The surface elevation response within the GOM consists of an initial setup in both the alongshore and onshore directions which breaks up into smaller scale circulations after the storm has passed.

## 7. Discussion: Comparison of model results with observations

Taken together, the numerical experiments described here suggest several characteristics of the transient wind-driven response in the MAB and the GOM which can be compared with recent field observations. The transient surface elevation and current fluctuations occurring in the model MAB and GOM regions are made up of both local and nonlocal responses—i.e., variations directly related to local geometry, topography and forcing conditions and those related to causes distant in time and/or space. Over most of the model MAB, the alongshore flow is primarily driven by the regional alongshore windstress component. The effective adjustment time scale there is O(10 h) so that a very crude quasi-steady response is observed in the moving storm experiments. Both coastal adjusted sea level and the alongshore transport lag the alongshore windstress by ~4–10 h. The transient response can also include localized normal modes of oscillation in both the New York Bight and GOM regions. These modes have discrete frequencies and exhibit southward phase propagation within the MAB. The transient circulation, although coherent over distances com-

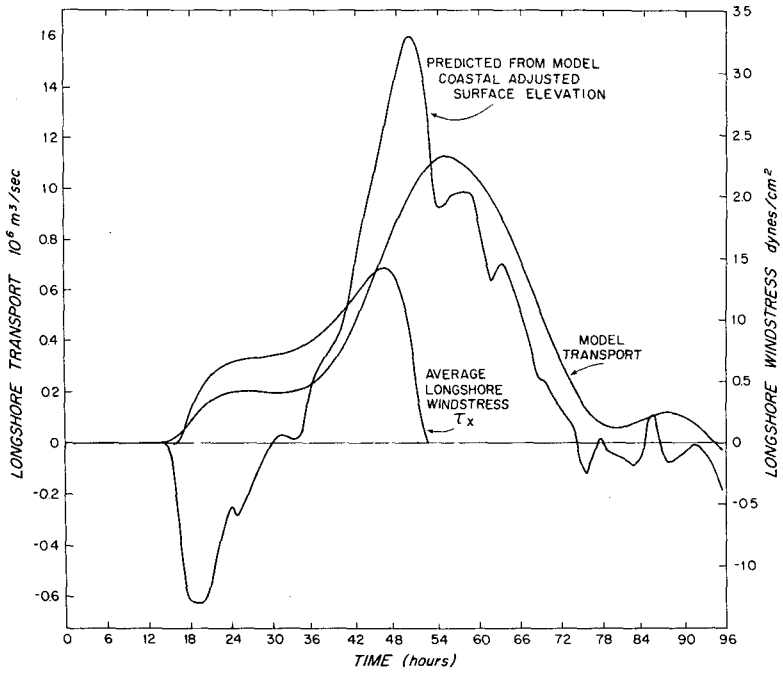


FIG. 21. Time history of the alongshore wind stress, the model total alongshore transport, and the alongshore transport predicted from coastal adjusted surface elevation at $i = 45$ in experiment MS2.

parable with the full length of the model MAB, is strongly influenced by variations in wind strength and direction caused by both the wind-stress pattern and the regional geometry and topography of the MAB. The transient response within the GOM is more complex due both to its more complex geometry and topography and to its much longer frictional adjustment time scale.

Some of these model characteristics can be seen in recent field observations made in the MAB and GOM. Flagg (1977); EG&G (1978); Bennett and Magnell (1979); Mayer *et al.* (1979); Butman *et al.* (1979); and Chuang *et al.* (1979) have examined the coherence between the local wind-stress and current components at different sites within the MAB and all find that the alongshore current response is essentially barotropic and highly coherent with the local alongshore wind stress component over the synoptic-scale (2–10 day) band. The observed phase lag between alongshore wind stress and current components varies from ~4 h nearshore to ~10 h over the outer shelf. Flagg (1977), Mayer *et al.* (1979), and Chuang *et al.* (1979) also found that the amplitude of the alongshore current fluctuations does not vary significantly in the cross-shelf plane (except in the bottom boundary layer) so that the observed alongshore transport fluctuations are coherent with the alongshore wind-stress variations with a phase lag of roughly 4–10 h. Using current data obtained on the New England shelf by Flagg (1977), we can crudely estimate the proportionality factor between the observed alongshore windstress and total transport to be $0.25 \pm 0.1 \times 10^6$ m$^3$ s$^{-1}$ dyn cm$^{-2}$. This compares favorably with the steady state model value of about $0.33 \times 10^6$ m$^3$ s$^{-1}$ dyn$^{-1}$ cm$^{-2}$ (shown in Fig. 15b) when the difference in coastline orientation is taken into account. As suggested in Figs. 3 and 12, EG&G (1978), Bennett and Magnell (1979), and Csanady (1979) have found that cross-shelf winds can set up trapped pressure fields which can drive alongshore currents within the shallower nearshore region of the New York Bight.

Beardsley *et al.* (1977) have examined the spatial structure of the synoptic-scale adjusted surface elevation fluctuations observed over the northern half of the MAB and find that the adjusted surface elevation fluctuations over the shelf are coherent and in phase with coastal adjusted surface elevation and have a monotonic cross-shelf structure with maximum amplitudes at the coast. The model results exhibit this behavior except well after the storms have passed in the moving storm experiments; however, the adjusted surface elevation fluctuations during this latter transient period have small amplitudes.

Wang (1979) and Noble and Butman (1979) have investigated the relationship between local wind stress and coastal adjusted surface elevation within the MAB. They find that north of Cape May, coastal adjusted surface elevation and the alongshore wind stress are highly coherent over the synoptic-scale band, and coastal adjusted surface elevation lags the

TABLE 2. Average adjusted surface elevation response for a nominal 1 dyn cm$^{-2}$ alongshore wind stress at coastal stations. Data adapted from Table 3 of Noble and Butman (1979).

| Station (*i* location) | Average adjusted surface elevation response for a 1 dyn cm$^{-2}$ alongshore wind stress (cm) | |
|---|---|---|
| Scotian Shelf | | |
| Halifax (102) | 10.3 | |
| Gulf of Maine | | |
| Eastport (97) | 5.9 | 9.8 ± 3.3 cm |
| Rockland (85) | 11.6 | |
| Portland (77) | 11.6 | |
| Mid Atlantic Bight | | |
| Nantucket (65) | 8.7 | |
| New York (40) | 16.3 | 17.2 ± 4.1 cm |
| Atlantic City (33) | 23.3 | |
| Cape May (26) | 16.5 | |
| Norfolk (8) | 17.9 | |
| Cape Hatteras (1) | 12.0 | |

local wind stress by 8 to 12 h, indicating that the alongshore transport and coastal adjusted surface elevation fluctuations are in phase to within a few hours. South of Cape May the observed coastal adjusted surface elevation response is more complicated. Both Wang (1979) and Noble and Butman (1979) find downcoast (southward) propagation of coastal adjusted surface elevation fluctuation in the synoptic-scale band which they attribute to possible free continental shelf waves. The estimated phase speed is of order 600 km day$^{-1}$. In both moving storm experiments, southward propagation of coastal adjusted surface elevation appears to occur during the relaxation phase after the storm has left the model domain (see Figs. 18 and 20). The estimated phase speed in these experiments is ~400 km day$^{-1}$. The relaxation phase of the numerical experiments can presumably be described by the normal modes of the model domain so that the southward phase propagation may be due to the characteristics of the lowest normal modes. Whether the phase propagation mechanisms implicit in the numerical model are representative of real-world phenomena is presently unclear, however.

These comparisons between model and field observations are primarily qualitative, however, and do not provide a critical test of model accuracy. A more quantitative comparison can be made between the coastal surface elevation response to alongshore wind stress reported by Noble and Butman (1979) and the equilibrium coastal surface elevation response predicted by the numerical model. We show in Table 2 and Fig. 15 the average adjusted surface elevation response for a nominal 1 dyn cm$^{-2}$ alongshore wind stress determined over the 0.04–0.4 cpd band at various coastal stations by Noble and Butman (1979). These values have been computed from the setup and setdown data given in Table 3 of Noble and Butman (1979) for an alongshore coastal wind speed squared of 100 m$^2$ s$^{-2}$. While the observed coastal response shown in Fig. 15 is larger than the model response, much of the difference is due to the offshore structure of the wind-stress field. The magnitude of the observed wind stress standard deviation increases in the offshore direction across the shelf by roughly 60% (Saunders, 1976) so that Noble and Butman (1979) who used coastal wind data underestimated the effective (i.e., across-shelf average) alongshore wind-stress component. To correct for this effect, we also show in Fig. 15 the average observed response divided by the factor 1.3, which crudely approximates the ratio of the average stress over the shelf to the coastal stress. The adjusted observed response and the equilibrium model response for $C_D\tau_x = 0.5 \times 10^{-2}$ show reasonable agreement in amplitude in the MAB and both responses exhibit a similar northward decrease in amplitude from the MAB to the GOM. The principal discrepancy occurs within the GOM where the model response is unrealistically limited by the open boundary condition ($\zeta = 0$) applied across the Scotian shelf. In the alongshore direction, Noble and Butman (1979) find a setup of 3.6 cm between Boston and Yarmouth for a 2 dyn cm$^{-2}$ alongshore wind stress; this compares to the model setup of 4.5 cm shown in Fig. 7.

The relationship between observed transport and wind stress are less clear within the GOM. Although Noble and Butman (1979) and Vermersch *et al.* (1979) find that coastal adjusted surface elevation is highly coherent with both windstress components over the entire GOM, Vermersch *et al.* (1979) report that the subtidal current fluctuations in the western GOM are only weakly correlated, if at all, with wind stress suggesting the importance of baroclinic processes in the deeper sections of the GOM. Butman (personal communication) also finds that the alongshore current fluctuations on the southern side of Georges Bank relatively are weak and only poorly correlated with alongshore windstress.

In summary, some results of these initial model experiments compare favorably with the wind-driven transient response observed in the MAB. A major difference occurs within the GOM, however, where the model surface elevation fluctuations are unrealistically limited in amplitude primarily by the open boundary condition imposed across the Scotian shelf. We have repeated the alongshore impulsive wind-stress experiment described in Section 5 with the derivative condition ($\partial\zeta/\partial x = 0$) applied on the Scotian and Cape Hatteras cross-shelf boundaries. Although the *initial* adjustment time scales within the MAB and GOM are not altered by

this derivative boundary condition, this modification introduces an additional *long* (order 2 day) adjustment time. It also causes an unrealistically large northward increase in the coastal surface elevation response to unit alongshore wind stress within the GOM. This result underscores the need for further research on the open boundary condition question before more quantitative comparisons can be made between model and observation. Additional work also is needed to facilitate the direct comparison of model and field data.

We hope, however, that these initial numerical experiments with a simple physical model will provide a good conceptual framework from which to examine systematically the sensitivity of these model results to both changes in the open boundary conditions and the model domain. The sensitivity of these results to changes in the model domain and more elaborate specifications of the open boundary conditions will be addressed in Part II of this study.

*Acknowledgments*. We would like to acknowledge J. Bennett who helped with the initial program development and H. Ou who helped analyze some of the initial model results. We also had several useful discussions with W. Brown and B. Butman about the model results and J. Allen made a careful review of the original manuscript. The numerical work was initiated at MIT under NSF Grants DES73-00528 and OCE74-03001A03 when both authors were members of the Meteorology Department. The work has been continued at WHOI under NSF Grants OCE76-01813, OCE78-19513, and OCE80-14941. Most of the computations were conducted at the National Center for Atmospheric Research which is supported by the National Science Foundation.

## REFERENCES

Allen, J. S., 1976: On forced, long continental shelf waves on an f-plane. *J. Phys. Oceanogr.*, **6**, 426–431.

Beardsley, R. C., and B. Butman, 1974: Circulation on the New England continental shelf: response to strong winter storms. *Geophys. Res. Lett.*, **1**, 181–184.

Beardsley, R. C., and C. D. Winant, 1979: On the mean circulation in the Mid-Atlantic Bight. *J. Phys. Oceanogr.*, **9**, 612–619.

——, H. Mofjeld, M. Wimbush, C. N. Flagg and J. A. Vermersch, Jr., 1977: Ocean tides and weather-induced bottom pressure fluctuations in the Middle-Atlantic Bight. *J. Geophys. Res.*, **82**, 3175–3182.

Bennett, J. R., and B. A. Magnell, 1979: A dynamical analysis of currents near the New Jersey coast. *J. Geophys. Res.*, **84**, 1165–1175.

Brown, W., W. Munk, F. Snodgrass, H. Mofjeld and B. Zetler, 1975: MODE bottom experiment. *J. Phys. Oceanogr.*, **5**, 75–85.

Butman, B., M. Noble and D. A. Folger, 1979: Long-term observations of bottom current and bottom sediment movement on the mid-Atlantic continental shelf. *J. Geophys. Res.*, **84**, 1187–1205.

Chuang, W.-S., D.-P. Wang and W. C. Boicourt, 1979: Low-frequency current variabilities on the southern Mid-Atlantic Bight. *J. Phys. Oceanogr.*, **9**, 1144–1154.

Csanady, G. T., 1974: Barotropic currents over the continental shelf. *J. Phys. Oceanogr.*, **4**, 357–371.

——, 1980: Longshore pressure gradients caused by offshore wind. *J. Geophys. Res.*, **85**, 1076–1084.

EG&G, 1978: Summary of physical oceanographic observations near the site of the proposed Atlantic generating station, offshore of Little Egg Inlet, New Jersey—1972 through 1976. Rep. to the Public Service and Gas Company, Newark, NJ 07101, 365 pp.

Flagg, C. N., 1977: The kinematics and dynamics of the New England continental shelf and shelf/slope front. Ph.D. thesis, MIT-WHOI Joint Program in Oceanography, Woods Hole, 207 pp.

Garrett, C., 1974: Normal modes of the Bay of Fundy and Gulf of Maine. *Can. J. Earth Sci.*, **11**, 549–556.

Hasse, L., 1974: A note on the surface-to-geostrophic wind relationship from observations in the German Bight. *Bound.-Layer Meteor.*, **6**, 197–201.

Kajura, K., 1958: Effect of Coriolis force on edge waves. (II) Specific examples of free and forced waves. *J. Mar. Res.*, **16**, 145–157.

Mayer, D. A., D. V. Hansen and D. A. Ortman, 1979: Long term current and temperature observations on the Middle Atlantic Shelf. *J. Geophys. Res.*, **84**, 1776–1792.

Mooers, C. N. K., J. Fernandez-Partagas and J. F. Price, 1976: Meteorological forcing fields of the New York Bight. University of Miami RSMAS Tech. Rep. TR76-8 (unpublished manuscript).

Mysak, L. A., 1980: Recent advances in shelf wave dynamics. *Rev. Geophys. Space Phys.*, **18**, 211–241.

Noble, M., and B. Butman, 1979: Low-frequency wind-induced sea level oscillations along the east coast of North America. *J. Geophys. Res.*, **84**, 3227–3236.

Platzman, G. W., 1972: Two-dimensional free oscillations in natural basins. *J. Phys. Oceanogr.*, **2**, 117–138.

Reid, R. O., 1958: Effects of Coriolis force on edge waves. (I) Investigation of the normal modes. *J. Mar. Res.*, **16**, 109–144.

Saunders, P. M., 1977: Wind stress on the ocean over the eastern continental shelf of North America. *J. Phys. Oceanogr.*, **7**, 555–566.

Smith, P. C., B. Petrie and C. R. Mann, 1978: Circulation, variability and dynamics on the Scotian Shelf and slope. *J. Fish. Res. Board Can.*, **35**, 1067–1083.

Uchupi, E., 1965: Map showing relation of land and submarine topography, Nova Scotia to Florida. USGS Misc. Geol. Invest. Map I-451.

Vermersch, J. A., R. C. Beardsley and W. S. Brown, 1979: Winter circulation in the western Gulf of Maine. Part 2: Current and pressure observations. *J. Phys. Oceanogr.*, **9**, 768–784.

Wang, D.-P., 1979: Low-frequency sea level variability in the Middle Atlantic Bight. *J. Mar. Res.*, **37**, 683–697.